A quasi-exponential distribution of interfacial voids and its effect on the interlayer strength of 3D printed concrete

Lewei He [a, b, 1], Bingzhi Chen [a, 1], Qimin Liu [c], Hao Chen [a], Hua Li [b], Wai Tuck Chow [b], Jiaoning Tang [d, e], Zhibin Du [a, *], Yang He [d, *], Jiahui Pan [a, *]

[a] *School of Software, South China Normal University, Guangzhou 510631, China*
[b] *School of Mechanical and Aerospace Engineering, Nanyang Technological University, Singapore 639798, Singapore*
[c] *School of Civil Engineering and Architecture, Wuhan University of Technology, Wuhan 430070, China*
[d] *School of Materials and New Energy, South China Normal University, Shanwei 516600, China*
[e] *Guangdong Research Center for Interfacial Engineering of Functional Materials, Shenzhen University, Shenzhen 518060, China*

ABSTRACT: In this work, a novel theoretical model of the void length probability distribution in 3D printed concrete is established based on a zigzag analog of the layer interface. A quasi-exponential distribution of void length is predicted and subsequently validated on both the zigzag analog and the actual 3D printed concrete, with different void ratios that determine the descending rate and node intervals that decide the horizontal scaling of the distribution. Moreover, the relationships between the interlayer strength, void ratio, and quantity of voids are also studied based on the theoretical model. It is found that the quantity of voids is symmetric about a void ratio of 0.5, and the decrease in the interlayer strength against the void ratio is non-linear which is approximated well by combined exponential and linear functions. This work is believed to reveal the nature of the interfacial void distributions and significantly advance the understanding of the layer interface in 3D printed concrete. The code for the zigzag analog with the computation of its interlayer strength is publicly available at: https://github.com/Human-HLW/Layer-interface.

Keywords: 3D Concrete printing; Interfacial void; Probability distribution; Interlayer strength; Fracture mechanics

---

* Corresponding authors.
E-mail addresses: zhibindu@126.com (Z. Du), heyang@m.scnu.edu.cn (Y. He), panjiahui@m.scnu.edu.cn (J. Pan)
[1] Lewei He and Bingzhi Chen are co-first authors of this paper.

1. Introduction

3D concrete printing, characterized by the extrusion of well-mixed concrete layer by layer according to the structural layout [1-3], is becoming increasingly popular in both the academic and construction sectors due to its many advantages, including increased productivity, improved worksite environment, reduced building waste, shortened project duration, and mass customization [4-6]. Meanwhile, large quantities of voids exist at the layer interface due to the nature of 3D concrete printing, such that strength and durability of the layer interface may decrease significantly compared with those of the layer matrix [7-10].

The forming of interfacial voids in 3D printed concrete is related to the material properties [11], nozzles [12], processes [13], and environmental conditions [14], while the fundamental generation mechanism of interfacial voids was assumed by Geng *et al.* [15] in the following two steps. First, the protruding areas on the surface make initial contact when the rough surfaces of the upper and lower concrete layers come into close proximity. Then, the contact areas on the surface expand due to the effects of deformation and flow, and thus enclose the concave areas and trap the interfacial voids as the concrete hardens. It was found that the interfacial voids generally exhibited an oblate spheroid shape along the interface with a void ratio between 0.1 and 0.4 [16-19], and the void ratio might grow with the roughness and stiffness of the underlying concrete due to a looser interlayer contact [20-23]. Moreover, a peak void length followed by a decaying long tail was widely observed at the interfaces within concrete [24-26] and other materials [27-30]. To the best of the authors' knowledge, the relationship between the interfacial void ratio and interlayer strength was only assumed to be linear according to the studies by Geng *et al.* [15], He *et al.* [10], Marchment *et al.* [31] and Wang *et al.* [32]. The theoretical probability distribution of

interfacial void length and its effect on the interlayer strength of 3D printed concrete have not yet been revealed.

Regarding the numerical techniques for the interfacial failure of 3D printed concrete, most researchers modeled the interface without explicitly addressing the presence of interfacial voids. He *et al.* [33] adopted the concrete damaged plasticity model for both the matrix and interface, and found that the interlayer strength was strongly affected by the interlayer notch depth. Xiao *et al.* [34] modeled the concrete interface by cohesive element with ultimate tensile and shear stresses, and noted that the compressive strength of 3D printed concrete was the highest along the printing direction because in this direction the interlayer shear load was the smallest. Haveer *et al.* [35] conducted simulations on three-point bending with an anisotropic-continuum model for the matrix and a coulomb-friction model for the interface, and the force-displacement curve matched well with those obtained by the experiments. In contrast, Chen *et al.* [36] considered the role of voids by converting the concrete CT-scan cross sections into a lattice model, and found that interlayer chemical adhesion had an important role in the interlayer strength when different curing conditions were applied.

In the present work, the probability distribution of the interfacial void length is theoretically derived based on a zigzag analog of the layer interface, and relationships are established between the interlayer strength, interfacial void ratio, interfacial void quantity and interface area. It is believed that this study will advance the understanding of interfacial voids and fill the research gap between the void characteristics and interlayer strength of 3D printed concrete.

78   **2.   Theoretical modeling of the interfacial void length**

79   *2.1. Interfacial voids based on the zigzag analog of layer interface*

80   In order to analyze the distribution of interfacial voids in 3D printed concrete, a

81   zigzag analog of the layer interface is proposed. As shown in Figure 1, the surface of

82   the overlay is represented by a horizontal line, while the underlay surface is simplified

83   into a zigzag line with the control nodes distributed in a constant horizontal interval L

84   and their heights following a normal distribution $N(0,1)$. When the overlay is

85   deposited on the underlay at a certain interface level, interfacial bond is formed in the

86   areas where the underlay is higher than the interface level, and interfacial voids

87   formed in the remaining areas where the underlay is lower than the interface level

88   [37]. The interface level also determines the void ratio r between the total void

89   length and the length of interface, such that $r < 0.5$ if the interface level is below 0

90   and $r > 0.5$ if the interface level is above 0. Therefore, one of the main tasks in this

91   work is to derive the theoretical probability distribution of the interfacial void length

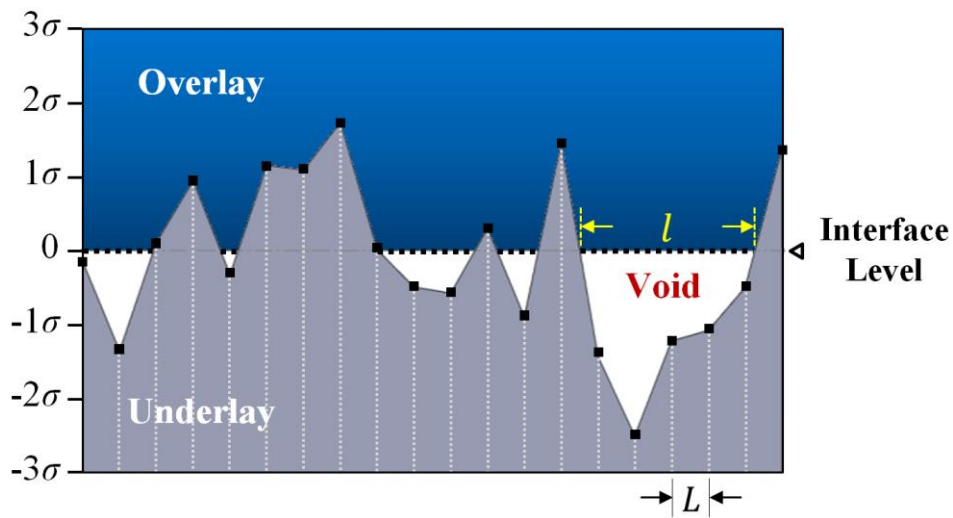92 l based on the zigzag analog of layer interface.

94   Figure 1. The zigzag analog of layer interface in 3D printed concrete with void length

95   l and node interval L

2.2. Distribution of the elementary void length l_0 subject to a void ratio of 0.5

97   The layout of an elementary void is illustrated in Figure 2(a) with the interface

98   level equal to 0 and void ratio $r = 0.5$, such that Nodes A and D are higher than the

99   level while Nodes B and C are lower than the level. Assuming that the node heights A

100   and B follow a normal distribution $N(0,1)$ as expressed in Equation (1), and that x

101   is the ratio between the two heights as expressed in Equation (2), then x follows a

102   Cauchy distribution from negative infinity to positive infinity and the probability

103   distribution function $f(x)$ is expressed by Equation (3). If we specify that both A

104   and B are positive by taking their absolute values with the direction of A pointing

105   upward and the direction of B pointing downward, x is then restricted to positive

106   values with Equation (3) updated to Equation (4).

$$A, B \sim N(0,1) \tag{1}$$

$$x = \frac{B}{A} \tag{2}$$

$$f(x) = \frac{1}{\pi(1 + x^2)} \tag{3}$$

$$f(x) = \frac{2}{\pi(1 + x^2)}, \qquad (x \geq 0) \tag{4}$$

107   If we assume that a is the horizontal distance between Node B and the left void tip,

108   the ratio x is also expressed by Equation (5) due to triangle similarity.

$$x = \frac{a}{L - a} \tag{5}$$

109   The derivative of Equation (5) is then expressed by

$$dx = \frac{L}{(L - a)^2} da \tag{6}$$

110   Since Equation (5) is monotonic and the values of a and x are in one-to-one

111   correspondence, the probability of x within dx should equal the probability of a

112   within da, which is expressed by

$$f(x)dx = g(a)da \tag{7}$$

113   where $g(a)$ is the probability distribution function of the length a. By substituting

114   Equations (4)~(6) into Equation (7), $g(a)$ is solved and expressed by

$$g(a) = \frac{2L}{\pi(L^2 - 2aL + 2a^2)}, \qquad (0 \leq a \leq L) \tag{8}$$

115   Independent node heights B and C are assumed for the convenience of formula

116   derivation, and thus b on the other side follows the same distribution as a. The

117   elementary void length l_0 is then defined by $a + b$, and its probability distribution

118   function $p(l_0)$ is computed by Equation (10).

$$l_0 = a + b \tag{9}$$

$$p(l_0) = \int_0^{l_0} g(a) \cdot g(l_0 - a)da, \qquad (0 \leq l_0 \leq 2L) \tag{10}$$

119   As shown in Figure 2(b), the plots of $g(a)$ and $p(l_0)$ are symmetric with higher

120   middle and lower sides, and their integrals over the function domains are equal to 1. It

121   is also observed that there is a certain probability of $a = 0$ (only if node height B is

122   0), while the probability of $l_0 = 0$ is negligible since it requires both B and C

123   equal to 0. So far, we have derived the length distribution function $p(l_0)$ of an

124   elementary void based on four nodes and void ratio $r = 0.5$. The next step is to

125   derive the length distribution function of an elongated void formed by multiple nodes.
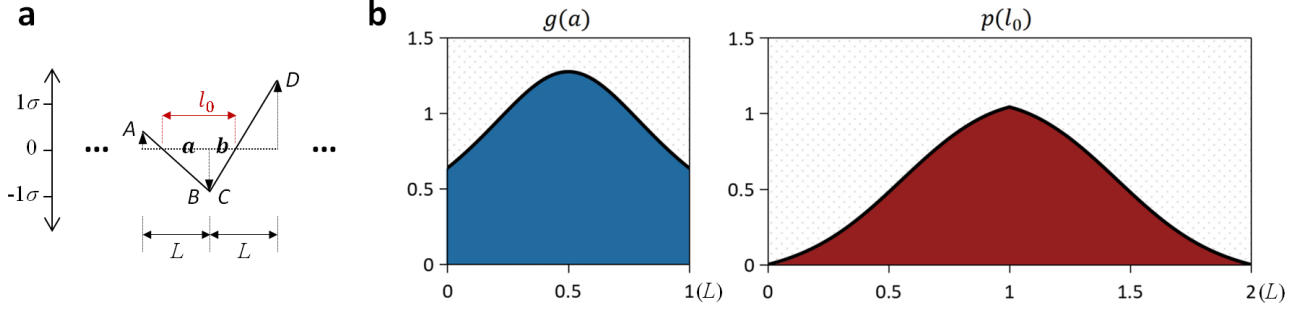
Figure 2. (a) Illustration of the elementary void length l_0 with Nodes A~D, and (b) probability distribution functions $g(a)$ and $p(l_0)$ with void ratio $r = 0.5$

2.3. Distribution of the elongated void length l subject to a void ratio of 0.5

As shown in Figure 3(a) for a void formed by multiple nodes with the interface level equal to 0 and void ratio $r = 0.5$, its length l_n is calculated by

$$l_n = l_0 + nL, \qquad (nL \leq l_n \leq nL + 2L) \tag{11}$$

where $n = 0, 1, 2 \cdots$ denotes the number of full intervals L that the void covers, demanding n extra nodes below the interface level with a probability of 0.5 for each node. Therefore, the length distribution function of an elongated void covering n full intervals L is expressed by

$$p(l_n) = p(l_0) \times 0.5^n, \qquad (nL \leq l_n \leq nL + 2L) \tag{12}$$

By summing Equation (12) over n, the length distribution function of a void with any void length $l \geq 0$ is expressed by

$$p(l) = k \sum_{n=0}^{\infty} p(l_n), \qquad (l \geq 0) \tag{13}$$

where $k = 0.5$ is a scaling coefficient to guarantee that the probability density function satisfies

7

$$\int_{l=0}^{\infty} p(l) = 1 \tag{14}$$

140   By simplifying the $p(l_0)$ illustrated in Figure 2(b) into a piecewise linear function,

141    $p(l)$ is plotted in Figure 3(b) and then further simplified into a quasi-exponential

142   distribution with a linear growth segment and an exponential decay segment

$$p(l) = \begin{cases} H \times \dfrac{l}{L}, & 0 \le l < L \\ H \times 0.5^{\frac{l-L}{L}}, & l \ge L \end{cases} \tag{15}$$

143   where the maximum value H is also a scaling coefficient to satisfy the constraint of

144   the probability density function, and H is expressed by
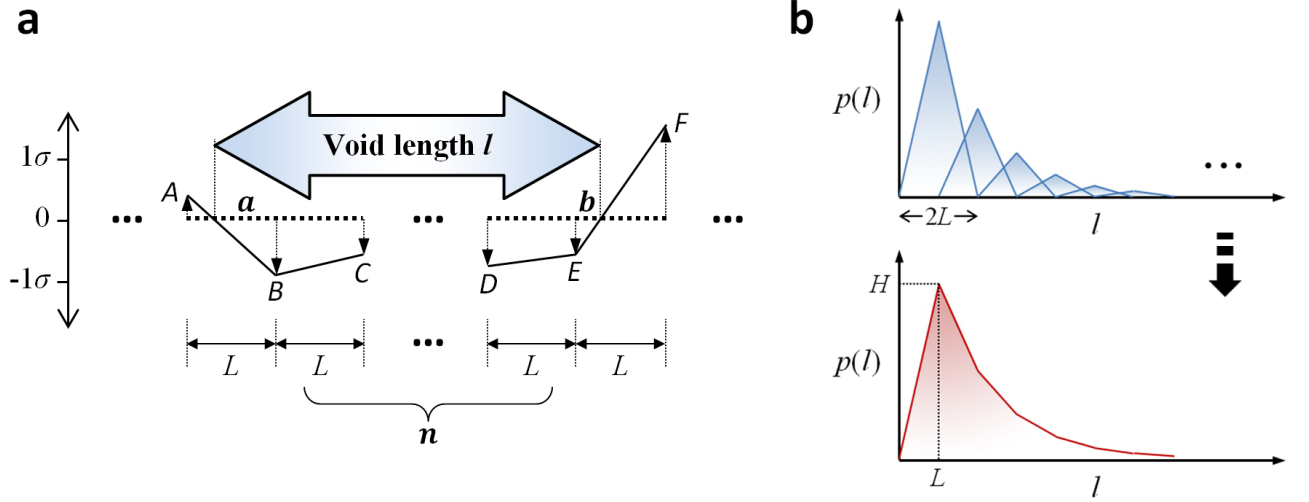
$$H = \frac{2 \times \ln 0.5}{(\ln 0.5 - 2)L} \tag{16}$$

145

146   Figure 3. (a) Illustration of an elongated void covering n full intervals L, and (b) probability

147   distribution of the void length l with void ratio $r = 0.5$

148   *2.4. Distribution of the elongated void length l with different void ratios*

149   With a general void ratio r that is different from 0.5, the exponential form of

150   Equation (12) still holds while the shape of $p(l_0)$ changes and 0.5 is replaced by r.

151   As shown in Figure 4(a), the average void length l becomes larger when r increases,

152   and smaller when r decreases. Therefore, it is assumed that the peak length of $p(l)$

153   shifts from L to λL and the shift factor λ is expressed by

$$\lambda = \lambda_0(r - 0.5) + 1 \tag{17}$$

154   where λ_0 denotes the influence of the void ratio r on the shift factor λ and

155       $\lambda_0 = 1.5$ is assumed in this model, as shown in Figure 4(b). The distribution of

156   interfacial void length l with different void ratios r is then expressed by

$$p(l) = \begin{cases} H \times \dfrac{l}{\lambda L}, & 0 \leq l < \lambda L \\ H \times r^{\frac{l-\lambda L}{L}}, & l \geq \lambda L \end{cases} \tag{18}$$

157   where the maximum value H is expressed by

$$H = \frac{2 \ln r}{(\lambda \ln r - 2)L} \tag{19}$$

158   In this model, the length distribution function $p(l)$ of interfacial voids consists of a

159   linearly increasing segment and an exponentially decreasing segment, and its shape

160   depends only on the node interval L and void ratio r, as shown in Figure 4(c). When

161   r is smaller, the peak length λL moves leftward with a higher maximum value H

162   and steeper increasing and decreasing segments, indicating that the void lengths l are

163   more concentrated around a smaller peak length. When r becomes larger, the peak

164   length λL moves rightward with a lower maximum value H, which suggests that l

165   are more spread with long voids more frequently observed. It is also demonstrated

166   that the peak length λL always falls between 0 and $2L$, since the length of elementary

167   void l_0 ranges from 0 to $2L$ and the incidence of elongated void decreases

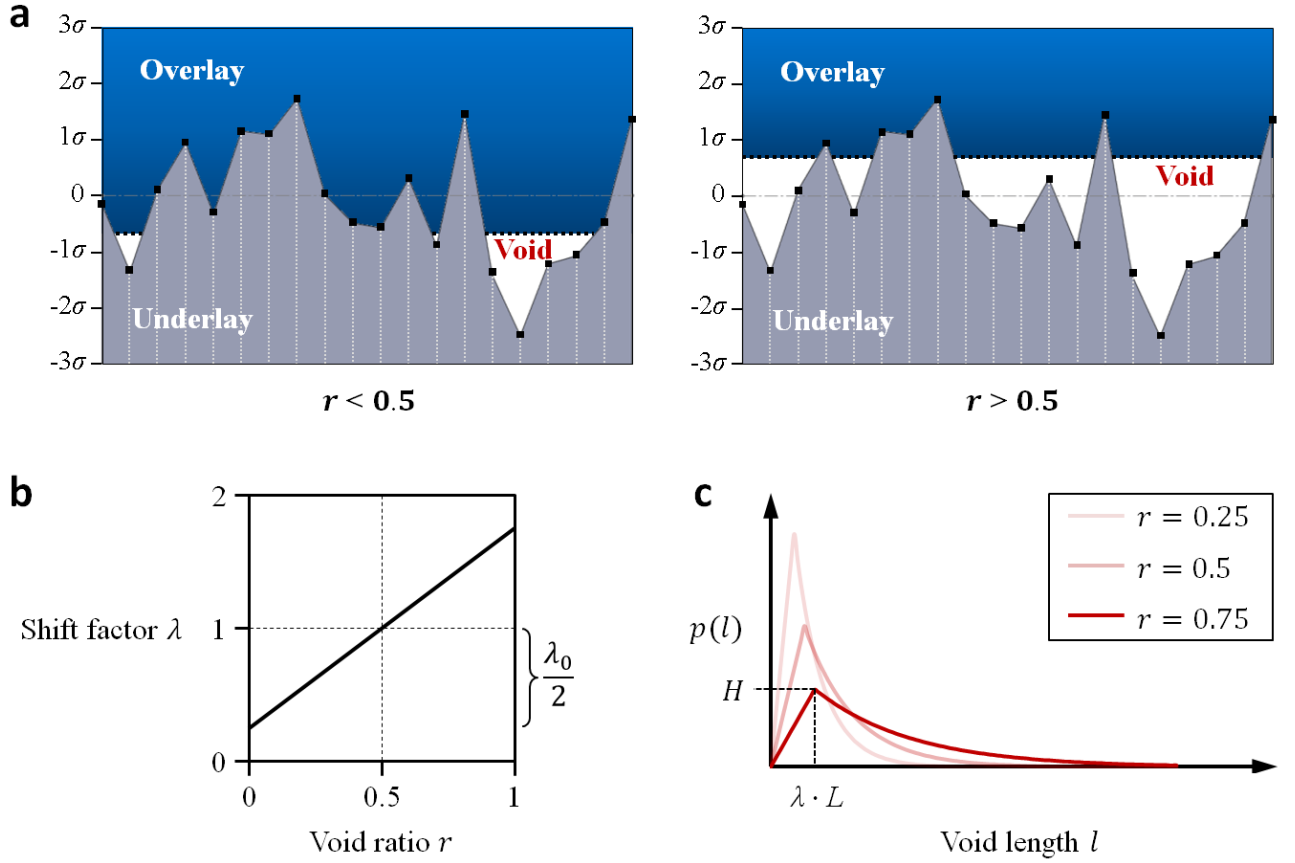168   exponentially with the number of full intervals covered by the void.

Figure 4. (a) The zigzag analog of layer interface with the void ratios $r < 0.5$ and $r > 0.5$, (b) relationship between the shift factor λ and void ratio r, and (c) the probability distributions of the void length l with different void ratios r

3. Verification of the theoretical model by the rough surface analog

In order to verify this model of the void length distribution in 3D printed concrete, one hundred million nodes with their heights following a normal distribution are generated in MATLAB R2020b, with a constant interval $L = 10$ units and a zigzag line connecting each pair of the neighboring nodes. A horizontal line goes through the zigzag line at different interface levels, and then interfacial voids are formed where the zigzag line is below the horizontal line. The interface levels are adjusted for three void ratios $r = 0.25$, $r = 0.5$ and $r = 0.75$, and then the interfacial void lengths are measured and plotted statistically with Equation (18) on both the normal and logarithmic scales, as shown in Figure 5, for a close comparison

183 of the length distributions between the simulation and theoretical model. Intersection

184 over union (IOU) is calculated for the distributions on the normal scale, and it is found

185 that the IOUs are greater than 80% in all the three scenarios, indicating a decent

186 overlap between the theoretical model and the simulation result across the entire

187 domain of the void length. On the logarithmic scale, the theoretical model in the

188 descending segment becomes linear due to its exponential nature, and the simulation

189 results with the void length $l > 2L$ are closely distributed around the theoretical

190 model with a correlation coefficient R^2 higher than 0.94. It is also seen that the

191 simulation results between 0 and $2L$ show some extent of discrepancy from the

192 theoretical model, probably because Nodes B and C in Figure 2(a) merge into one

193 node for an elementary void, while in the derivation of theoretical model they are

194 simplified into two independent nodes. In this section, the theoretical model of the

195 void length probability distribution is verified through MATLAB simulation based on

196 a zigzag analog of layer interface, and the next section further validates the model via

197 the experimental results of 3D printed concrete.
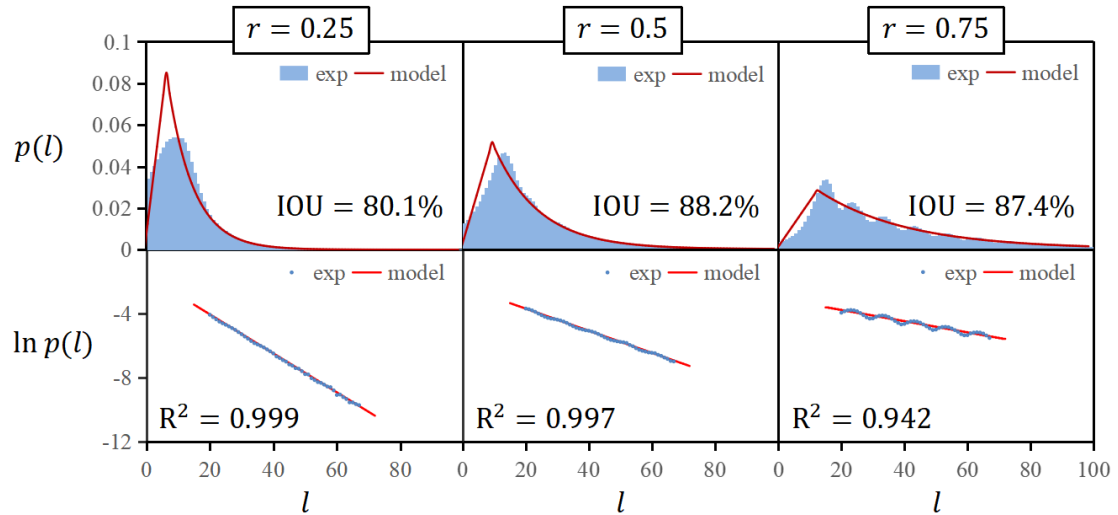

198

199 Figure 5. Comparison of the void length distributions between the simulation and

200 theoretical model with $L = 10$ units on both the normal and logarithmic scales

201 **4. Validation of the theoretical model on 3D printed concrete**

202 *4.1. Sample collection*

203   The samples for validation of the theoretical model are collected from two 3D

204 printed concrete materials that are summarized in Table 1, with totally different mix

205 designs and printing parameters. More details on the material preparation and printing

206 processes are provided in Ref. [10] for Material 1 and Ref. [12] for Material 2.

207 Samples 1, 2 and 3 are cropped from Material 1 in a single batch at different locations,

208 while the samples Rec-2, Rec-3 and Rec-4 are printed by Material 2 with the

209 corresponding nozzle shapes. The surface and interfacial void characteristics of

210 Materials 1 and 2 are analyzed thoroughly in the following sections.

211 Table 1. Specifications of the samples printed by Materials 1 and 2

	Mix design	OPC	FA	SF	Sand	Water	SP
	(weight %)	26.32	7.52	3.76	45.11	17.29	0
Mater. 1	Printing parameter	Nozzle direction		Translation speed	Flow rate		Nozzle distance
		Horizontal		8 cm/s	36 cm^3/s		0.5 cm
	Label	Sample 1	Sample 2	Sample 3	(by sample location)		
	Mix design	OPC	FA	SF	Sand	Water	SP
	(weight %)	74.19	0	8.02	0	17.23	0.11
Mater. 2	Printing parameter	Nozzle direction		Translation speed	Flow rate		Nozzle distance
		Vertical		6 cm/s	28.8 cm^3/s		1.2 cm
	Label	Rec-2	Rec-3	Rec-4	(by nozzle shape)		

212   *4.2. Modified discrete Fourier transform (mDFT) of the surface*

213   To reveal the fundamental node interval L of the sample surfaces, modified

214   discrete Fourier transform (mDFT) is proposed in this work. Since a larger

215   wavelength usually leads to a greater height variation on the concrete surface, the

216   amplitude of a wavelength after DFT is divided by the wavelength and then scaled

217   from 0 to 1 for the relative intensity. Before the analysis of the sample surfaces,

218   mDFT is conducted first on 10-meter zigzag lines with a resolution of 10 μm and their

219   nodes following a normal distribution in height and separated by different horizontal

220   intervals $L_1 = 50$, $L_2 = 100$, $L_3 = 150$ and $L_4 = 200$ (μm) through MATLAB.

221   As shown in Figure 6 for the mDFT results of the four zigzag lines, the relative

222   intensities rise quickly to the maximum at the peak points $F_1 = 135$, $F_2 = 280$,

223    $F_3 = 400$ and $F_4 = 520$ (μm), and then fade gradually as the wavelength becomes

224   larger. If the node intervals L and the corresponding mDFT peak points F are

225   plotted together, it is found that F and L follow a linear relationship expressed by

$$F = 2.65L \tag{20}$$

226   With this relationship, it is then possible to conduct mDFT on the profiles of the

227   sample surfaces and calculate their representative node intervals L.
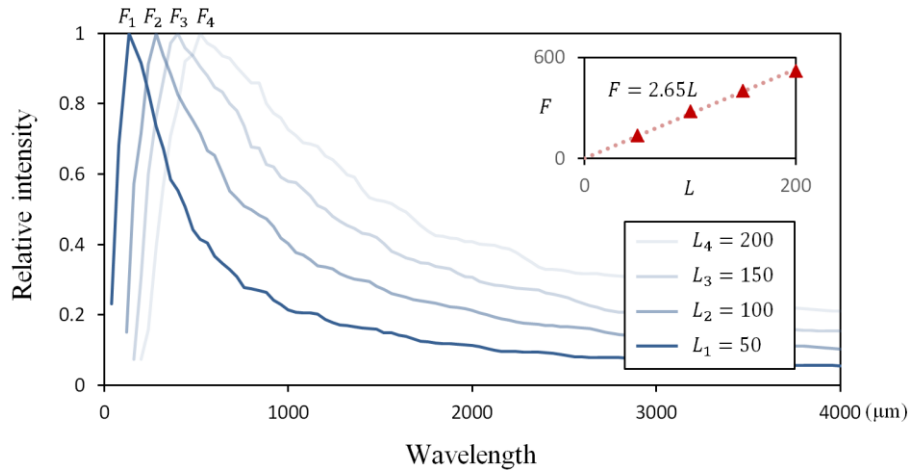

228

229   Figure 6. mDFT results of the zigzag lines with node intervals L equal to 50 ~ 200 μm
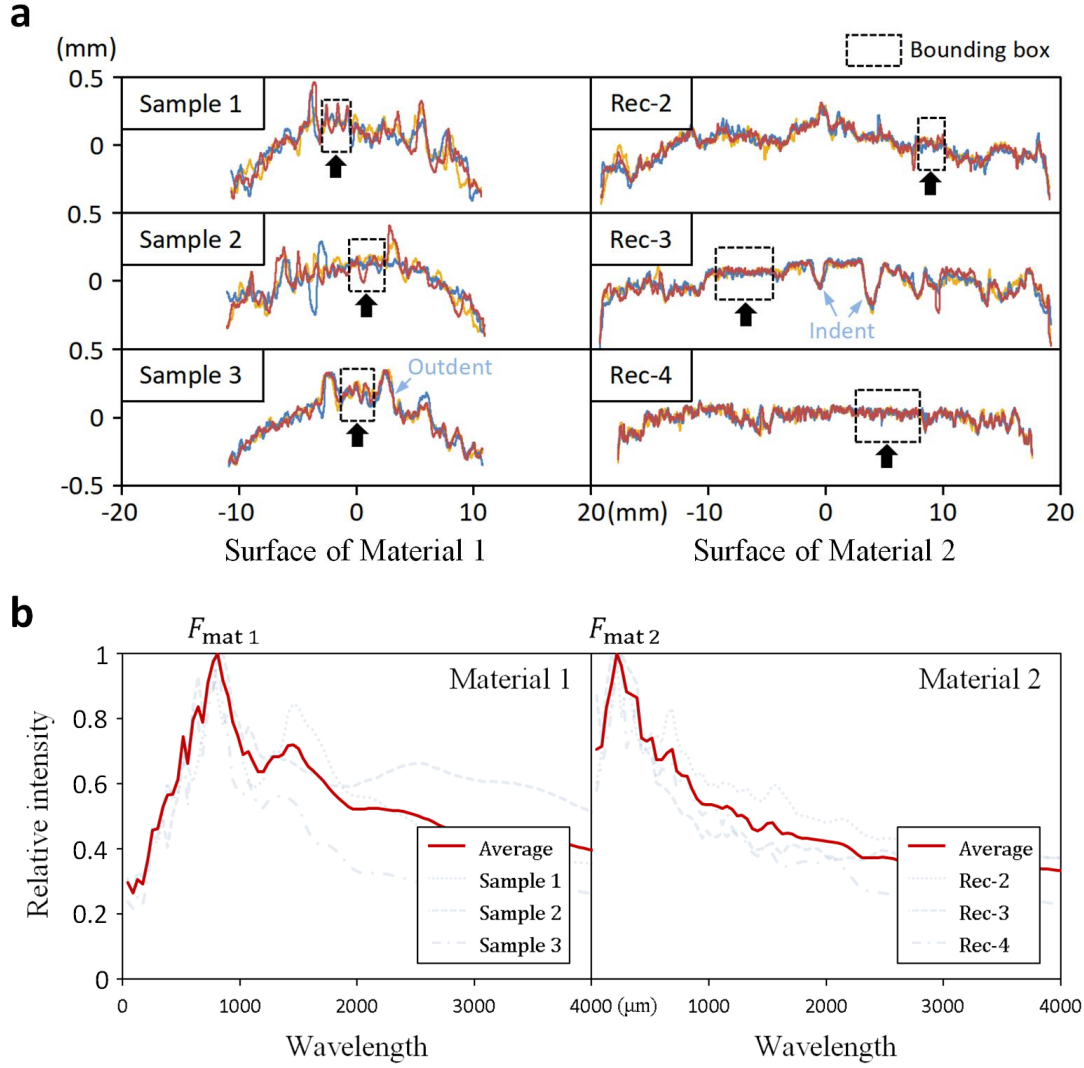
Figure 7. (a) The surface profiles and (b) mDFT results produced by Materials 1 and 2

The surface of each sample in Table 1 is measured by Keyence VK-X3000 laser microscopy system with an output resolution of 10.7 μm, and 180 cross-sectional profiles are recorded for each sample with three of them marked in red, blue and yellow, as shown in Figure 7(a). It is found that the surfaces are uneven with extrusion indents and outdents characterized by deviated and highly overlapped segments. To retrieve the node interval L that reflects the real surface characteristics, a region with relatively even profiles and free of extrusion indents and outdents is selected for each sample and marked by a bounding box. For each cross-sectional profile, a segment is truncated with random starting and ending points in the bounding box, and many

242 segments are concatenated together until the total length is more than thirty thousand

243 pixels. Subsequently, the mDFT technique is applied to the 180 concatenated profiles

244 of each sample for the intensity-wavelength relationship. As shown in Figure 7(b), the

245 mDFT results appear similar with close peak points for Material 1 and Material 2,

246 respectively, and thus they are averaged for each material with the obtained peak

247 points $F_{\text{mat1}} = 790\,(\mu\text{m})$ and $F_{\text{mat2}} = 214\,(\mu\text{m})$. The node intervals $L =$

248 $298\,(\mu\text{m})$ for Material 1 and $L = 81\,(\mu\text{m})$ for Material 2 are then calculated by

249 Equation (20) and substituted into Equations (18) and (19) for the theoretical void

250 length distributions.

251 *4.3. Measurement of the interfacial void length*

252 To measure the actual interfacial void length and validate the theoretical model,

253 layer interfaces of the 3D printed concrete samples are photographed seamlessly by

254 Keyence VK-X3000, including 16 interfaces in Material 1 with a resolution of 2.8 μm,

255 and 9 interfaces in Material 2 equally contributed by the Rec-2, Rec-3 and Rec-4

256 scenarios with a resolution of 1.4 μm. As shown in Figure 8, a green marker is

257 manually inserted in each interfacial void, and MATLAB code is used to locate the

258 interfacial voids by the green markers and calculate the length l of each interfacial

259 void. Thereafter, void ratio r is calculated by the sum of l over $W \times n$ as the

260 product of interface length and number of samples, namely $r = 0.372$ for Material 1,

261 $r = 0.473$, $r = 0.086$ and $r = 0.195$ for Material 2 in the Rec-2, Rec-3 and Rec-4

262 scenarios. The specifications of the interfacial voids in each scenario are summarized
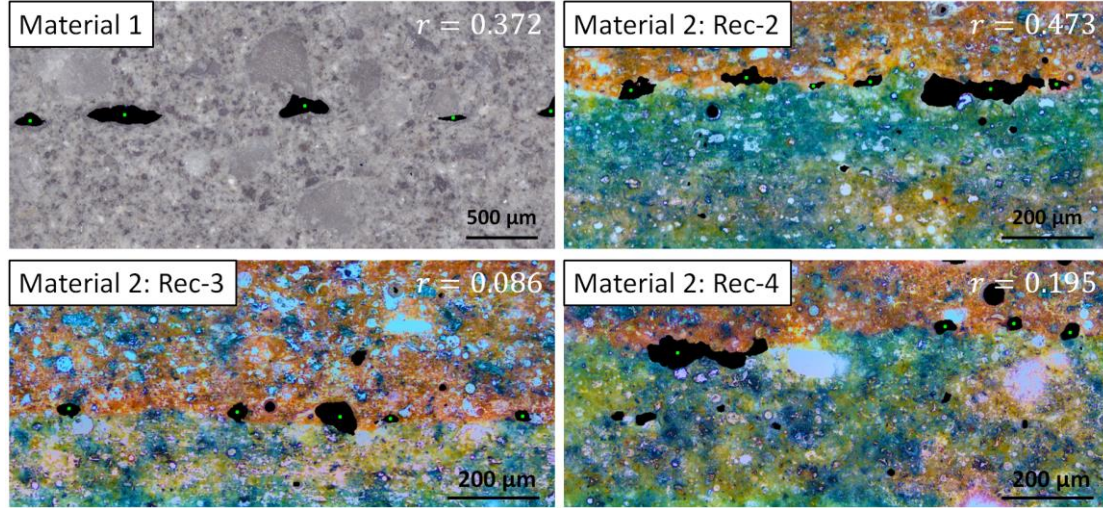
263 in Table 2.

Figure 8. Microscopic photographs of the sample cross sections with a green marker inserted in each interfacial void

Table 2. Specifications of the interfacial voids in Materials 1 and 2

	Node interval (L)	Scenario	Number of samples (n)	Quantity of voids (N)	Interface length (W)	Void ratio (r)
Mater. 1	298 μm	-	16	279	22 mm	0.372
Mater. 2	81 μm	Rec-2	3	425	37 mm	0.473
		Rec-3	3	227	37 mm	0.086
		Rec-4	3	268	38 mm	0.195

4.4. Validation by intersection over union (IOU) and linear regression

The distribution histogram of the measured void length l is plotted together with Equation (18) in the theoretical model based on the node interval L and void ratio r that are calculated in the previous sections. As shown in Figure 9(a) for the results of Material 1, the probability distribution of l resembles the theoretical model by increasing rapidly to the maximum and then decreasing gradually when l becomes larger, with an intersection over union IOU = 56.3% between the experimental observation and the theoretical model. It is also found that the peak

16

276 length in the histogram is smaller than that in the theoretical model, probably because

277 the void length distribution is slightly affected by the printing process, due to the

278 interlayer stresses and the fact that the overlay is deposited from one side to the other

279 with a certain interlayer contact angle. Moreover, the void length distribution on the

280 logarithmic scale is well fitted by a linear relationship with a correlation coefficient

281 $R^2 = 0.8033$. As shown in Figure 9(b) for the results of Material 2, the IOUs are

282 59.6%, 65.6% and 62.0% in the Rec-2, Rec-3 and Rec-4 scenarios, with R^2 equal to

283 0.8720, 0.9908 and 0.8323. Therefore, the quasi-exponential probability distribution

284 of the interfacial void length l characterized by its exponential nature is validated

285 successfully by the experimental observations.
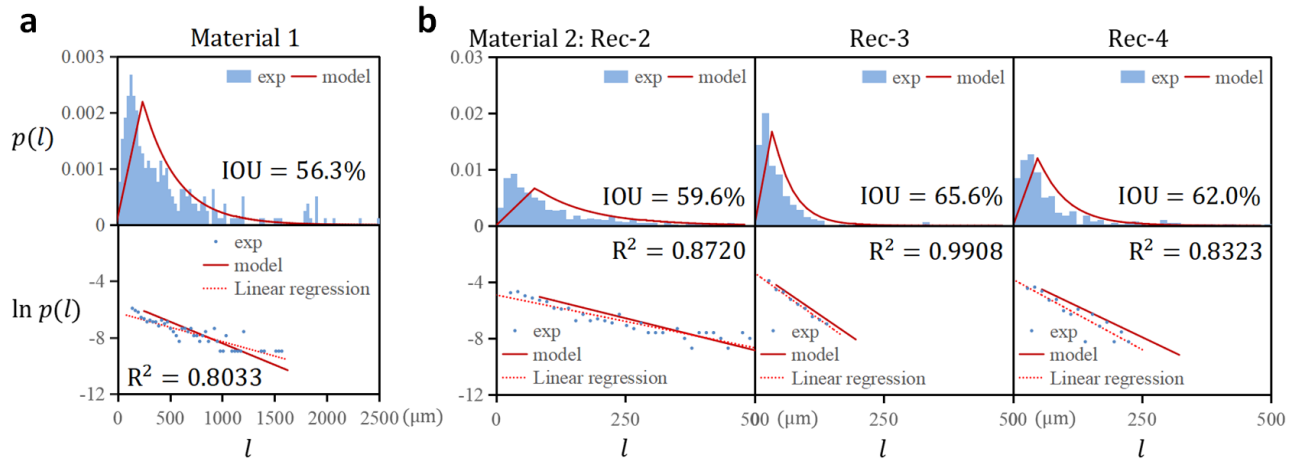

287 Figure 9. Comparison of the interfacial void length distributions between the experimental
288 observations and the theoretical model for (a) Material 1 and (b) Material 2

289 **5. Case studies and discussions**

290 In this section, supplementary case studies are conducted in order to gain a

291 deeper understanding of the theoretical model in respect of the relationships between

292 the interface level, the void ratio, and the quantity of voids.

293   *5.1. Effect of the interface level on the void ratio*

294   Different interface levels are selected from -2σ to 2σ, where σ represents the

295   standard deviation of the node height in the zigzag analog of interface, and then

296   MATLAB code is used to calculate the interfacial void ratio r based on 10 million

297   nodes. As shown in Figure 10, void ratio r against the interface level is plotted

298   together with the normal cumulative distribution functions NCDF $(0, \sigma)$ and

299   NCDF $(0, 0.8\sigma)$, where 0, σ and 0.8σ represent the expectation and the standard

300   deviations. NCDF $(0, \sigma)$ is also interpreted as the probability that a node is below the

301   interface level with formation of local void. However, the void ratio r deviates from

302   NCDF $(0, \sigma)$ but aligns more closely with NCDF $(0, 0.8\sigma)$. This observation is

303   explained by Figure 4(a) that when the interface level is low, the average distance

304   from the level to the nodes below it is smaller than that to the nodes above it.

305   Therefore in this scenario, the elementary void length l_0 on average is smaller than

306   the node interval L, and thus the resulted void ratio r is also smaller than the void

307   formation probability NCDF $(0, \sigma)$. On the contrary, the elementary void length l_0

308   on average is larger than L when the interface level is high, and thus the resulted

309   void ratio r is larger than the void formation probability NCDF $(0, \sigma)$. As a

310   consequence, the void ratio r in Equations (18) and (19) should be replaced by

311   NCDF $(0, \sigma)$, with updated Equations (21) and (22) which are actually used in Figures

312   5 and 9,

$$p(l) = \begin{cases} H \times \dfrac{l}{\lambda L}, & 0 \leq l < \lambda L \\ H \times q^{\frac{l-\lambda L}{L}}, & l \geq \lambda L \end{cases} \tag{21}$$

313   and

$$H = \frac{2 \ln q}{(\lambda \ln q - 2)L} \tag{22}$$

314   where q represents the void formation probability $\text{NCDF}(0, \sigma, level)$ subject to an

315   interface $level$ which is estimated by the void ratio r via the inverse normal

316   cumulative distribution function $\text{NCDF}^{-1}(0, 0.8\sigma, r)$, namely

$$q = \text{NCDF}\big(0, \sigma, \text{NCDF}^{-1}(0, 0.8\sigma, r)\big) \qquad (23)$$
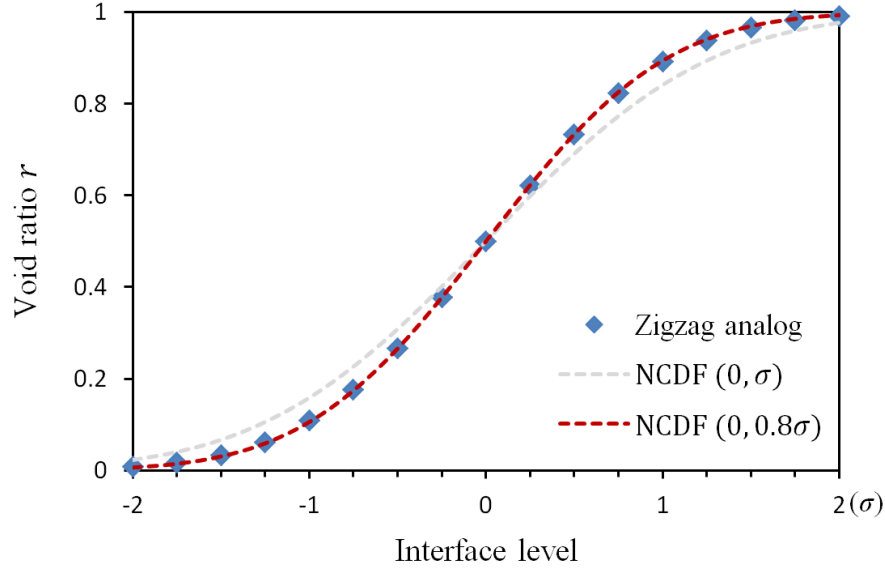

317

318 Figure 10. Relationship between the interface level and void ratio r in comparison

319   with the normal cumulative distribution functions $\text{NCDF}(0, \sigma)$ and

320                 $\text{NCDF}(0, 0.8\sigma)$

321 *5.2. Effect of the void ratio on the quantity of voids*

322   To predict the quantity of voids at a particular interface, non-dimensional metric

323 $N/(n \times W/L)$ is designed by the quantity of voids N/n over the quantity of node

324 intervals W/L across an interface. Different void ratios r from 0 to 1 are selected,

325 and MATLAB is used to construct the zigzag analog of interface based on 10 million

326 nodes in each scenario and calculate the corresponding void quantity metric. As

327 shown in Figure 11, $N/(n \times W/L)$ is symmetrical about $r = 0.5$, probably because

328 the quantity of voids equals the quantity of ligaments among them, and thus the voids

329 and ligaments are interchangeable by swapping the positions and replacing r with

330 $1 - r$. It is also seen that the metric $N/(n \times W/L)$ reaches its maximum of 0.25

331 when $r = 0.5$, which is theoretically derivable by the total void length over the void

332 length expectation. When r shifts from 0.5 to 0 or 1, the quantity of voids decreases

333 slowly at the beginning and then drops faster toward 0, since no void is formed with

334 $r = 0$ and no ligament formed with $r = 1$. Moreover, $N/(n \times W/L)$ produced in

335 the four scenarios with Materials 1 and 2 are also calculated according to Table 2 and

336 then plotted in Figure 11. It is seen that the result in Material 1 is well predicted by the

337 model, while some of the results in Material 2 are higher than the model predictions.

338 This discrepancy is attributed to the fact that in Material 2, interfacial voids also

339 originated from surfaces defects, such as air bubbles characterized by a higher

340 sphericity and pores that root deeply into the matrix, which are not accounted in the
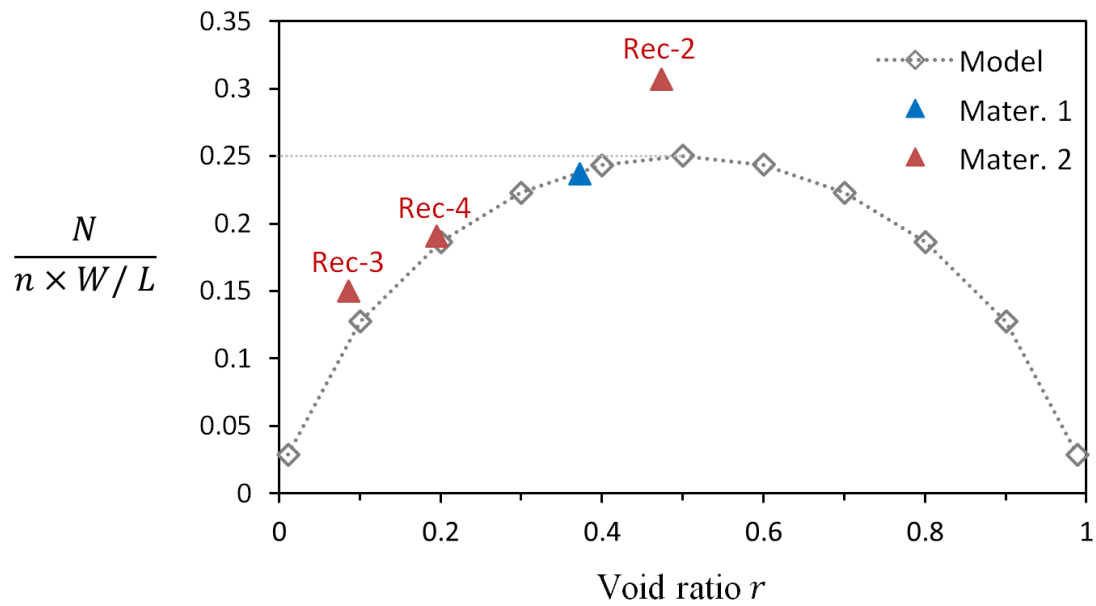
341 theoretical model.

342

343 Figure 11. Relationship between the void ratio r and non-dimensional void quantity

344 metric $N/(n \times W/L)$ which is composed of the quantity of voids N, the

345 number of samples n, the interface length W, and the node interval L

6. Relationship between the interfacial void ratio and interlayer strength

In order to compute the corresponding interlayer strength generated by the novel zigzag analog of interface, self-consistent superposition technique based on the fracture mechanics of brittle material is adopted due to its advantages in efficiency and accuracy [38]. By taking two cracks as an example, collinear cracks A and B are under remote tensile stress σ, as shown in Figure 12(a), with coordinates X_{A1} and X_{A2} for the two tips of Crack A and X_{B1} and X_{B2} for the two tips of Crack B. The self-consistent superposition technique regards this single problem as two equivalent problems. In Q1, only Crack A exists with distributed load P_A, while in Q2, only Crack B exists with distributed load P_B. The distributed load P_A on Crack A equals the superposed stress field induced by both the P_B on Crack B and remote stress σ, denoted by

$$P_A = \sigma + \Lambda_{AB} P_B \tag{24}$$

where Λ_{AB} represents the stress transmission function from Crack B to Crack A. If P_B is replaced by its average $\overline{P_B}$, P_A is approximated by

$$P_A \approx \sigma + \Lambda_{AB} \overline{P_B} \tag{25}$$

with the transmission function Λ_{AB} known in the closed form

$$\Lambda_{AB} = \frac{|2x - X_{B1} - X_{B2}|}{2\sqrt{(x - X_{B1})(x - X_{B2})}} \tag{26}$$

To solve $\overline{P_B}$ in Equation (25), the average is taken on both sides of the equation, namely

$$\overline{P_A} \approx \sigma + \overline{\Lambda_{AB} P_B} \tag{27}$$

where $\overline{\Lambda_{AB}}$ is simply a geometric property indicating the average stress at the

364   position of Crack A generated by one unit of uniform load on Crack B, calculated by

$$\overline{\Lambda_{AB}} = \frac{\left|\sqrt{(X_{A1}-X_{B1})(X_{A1}-X_{B2})} - \sqrt{(X_{A2}-X_{B1})(X_{A2}-X_{B2})}\right| + X_{A1} - X_{A2}}{X_{A2}-X_{A1}} \quad (28)$$

365   Similarly, the analysis also applies to Crack B by swapping A and B in Equations

366   (24)~(28), and $\overline{P_B}$ is then expressed by

$$\overline{P_B} \approx \sigma + \overline{\Lambda_{BA}P_A} \quad (29)$$

367    $\overline{P_A}$ and $\overline{P_B}$ are thus solvable by the following second-order matrix equation based on

368   Equations (27) and (29)

$$\begin{bmatrix} 1 & -\overline{\Lambda_{AB}} \\ -\overline{\Lambda_{BA}} & 1 \end{bmatrix} \begin{pmatrix} \overline{P_A} \\ \overline{P_B} \end{pmatrix} \approx \begin{pmatrix} 1 \\ 1 \end{pmatrix} \sigma \quad (30)$$

369   Hence, the distributed load P_A is solved by Equation (25). The stress intensity factors

370   SIF_{A1} at the left tip and SIF_{A2} at the right tip of Crack A are then computed by the

371   following equations with the numerical integration solution provided in Ref. [39].

$$SIF_{A1} = \frac{1}{\sqrt{\pi(X_{A2}-X_{A1})/2}} \int_{A_1}^{A_2} P_A(x) \frac{(X_{A2}-x)^{1/2}}{(x-X_{A1})^{1/2}} dx \quad (31)$$

$$SIF_{A2} = \frac{1}{\sqrt{\pi(X_{A2}-X_{A1})/2}} \int_{A_1}^{A_2} P_A(x) \frac{(x-X_{A1})^{1/2}}{(X_{A2}-x)^{1/2}} dx \quad (32)$$

372   For the problem with N cracks, SIFs are computed in the same process, with

373   Equation (25) modified to

$$P_A \approx \sigma + \Lambda_{AB}\overline{P_B} + \cdots + \Lambda_{AN}\overline{P_N} \quad (33)$$

374   and Equation (30) is modified to

$$\begin{bmatrix} 1 & -\overline{\Lambda_{AB}} & \cdots & -\overline{\Lambda_{AN}} \\ -\overline{\Lambda_{BA}} & 1 & \cdots & -\overline{\Lambda_{BN}} \\ \vdots & \vdots & & \vdots \\ -\overline{\Lambda_{NA}} & -\overline{\Lambda_{NB}} & \cdots & 1 \end{bmatrix} \begin{pmatrix} \overline{P_A} \\ \overline{P_B} \\ \vdots \\ \overline{P_N} \end{pmatrix} \approx \begin{pmatrix} 1 \\ 1 \\ \vdots \\ 1 \end{pmatrix} \sigma \quad (34)$$

375   This self-consistent superposition technique is encoded into a MATLAB program

376   called "Solving_cracks", and its solution for two equal-length collinear cracks is

377   compared with the exact solution in terms of α as the ratio between the SIF of the

378   two cracks and that of a single crack. Here, the void ratio r is defined by the length

379   of each crack over the distance between two crack centers. As shown in Table 3, the

380   relative error is lower than 3% when $r < 0.9$ and lower than 15% when $r < 0.98$,

381   indicating the capability of this technique to compute the SIF based on the novel

382   zigzag analog of interface.

383   Table 3. Comparison of α between the exact solution and that by the computer
384   program for two equal-length collinear cracks, with α defined by the stress intensity
385   factor SIF of the two cracks over that of a single crack

	α (Inner tips)			α (Outer tips)		
r	Exact	Solving_cracks	Error %	Exact	Solving_cracks	Error %
0.67	1.112	1.098	1.276	1.052	1.039	1.238
0.82	1.255	1.233	1.722	1.086	1.073	1.200
0.90	1.473	1.429	3.009	1.120	1.105	1.334
0.96	1.905	1.770	7.098	1.159	1.141	1.582
0.98	2.372	2.076	12.475	1.184	1.162	1.888

386   To study the relationship between the interlayer strength and interfacial void ratio,

387   relative strength S [40] is proposed as the ratio between the interlayer strength and

388   the strength of an "ideal" matrix with only a single crack of length L, calculated by

389   SIF of the crack with length L over the maximum SIF of the interfacial voids

390   generated by the novel zigzag analog,

$$S = \frac{\sigma\sqrt{\pi L/2}}{max(SIF)} \tag{35}$$

391   It was reported in Ref. [41] that the strength of concrete material is inversely

392   correlated with the specimen dimension, since the strength is largely dependent on the

393   "weakest link", and more extreme void lengths and distances are observed in larger

394   materials with the same void distribution. Therefore, a parameter defined by the

395   interface length W over the node interval L is proposed to characterize the interface

396   area. Relative interlayer strength S against void ratio r subject to $W/L = 100$,

397    $W/L = 500$ and $W/L = 2500$ is then computed by "Solving_cracks" and plotted in

398   Figure 12(b), with each data point based on 20 thousand samples produced by the

399   interface zigzag analog. It is found that there is a clear distinction between the three

400   W/L levels, such that the strength S with smaller W/L is higher than that with

401   larger W/L. Moreover, the strength S decreases non-linearly against the void ratio r,

402   at a higher rate when r is small and at a lower rate when r is large, which revises

403   the assumption of a linear decrease in Refs. [10, 15, 31, 32] and implies the

404   importance to reduce the void ratio even when it is not prominent. In particular, the

405   relationship within $0.05 \leq r \leq 0.6$ is well fitted by a combination of the exponential

406   and linear functions with a relative error below 5%.

407   Furthermore, S in the Rec-2 and Rec-3 scenarios subject to $W/L = 457$ due to

408   adhesive failure without the interlayer notch are also calculated by the interlayer

409   strengths over the matrix strength and then plotted in Figure 12(b). Meanwhile, those

410   in the other two scenarios are absent, since the interlayer strength is impacted by the

411   degraded interfacial adhesion in Material 1 [10] and no adhesive failure is observed in

412   the Rec-4 scenario with Material 2 [12]. It is seen that S in the Rec-2 and Rec-3

413   scenarios ($W/L = 457$) match well with the model predictions under $W/L = 500$.

414   Therefore, both the quasi-exponential probability distribution of the interfacial void

415 length and the relationship between the interfacial void ratio and interlayer strength

416 are validated successfully with a solid foundation provided for the optimization of

417 additive manufacturing processes. Further studies are also encouraged to consider the

418 degradation of interfacial fracture toughness and the crack detour due to various

419 interface geometries and surface roughness, in order to enhance the model's
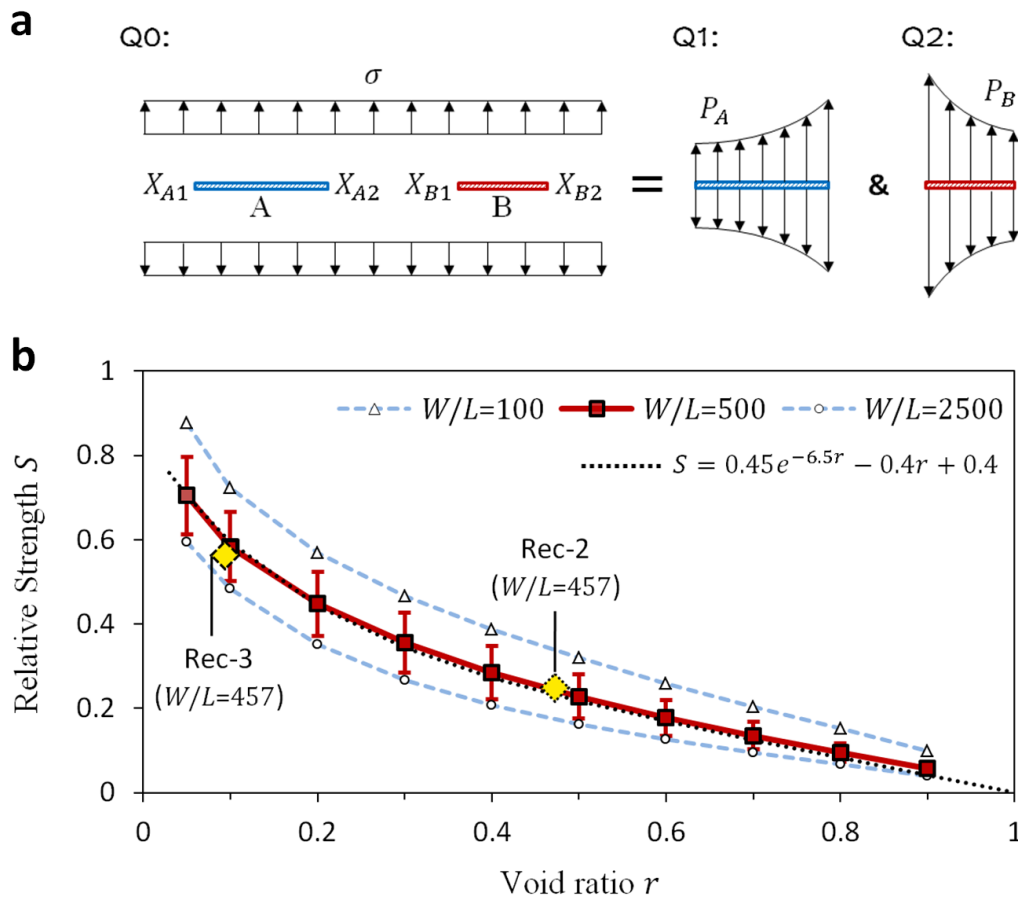
420 applicability and generalizability in the field of 3D concrete printing.

421

422

423 Figure 12. (a) Cracks A and B under remote tensile stress σ and the equivalent

424 problems Q1 and Q2 with distributed loads P_A and P_B to be solved, and (b)

425 relationship between the relative strength S and interfacial void ratio r

426 based on three interface W/L levels, with the Rec-2 and Rec-3 scenarios in

427 the experiment and the fitting function for $W/L = 500$

7. Conclusions

The present study develops a novel theoretical model of the interfacial void length distribution in 3D printed concrete, by simplifying the underlay surface into a zigzag line with constant node interval and normal distributed node height. Based on the theoretical model and careful cross-validations by both the simulation and experiment, several important conclusions are drawn and listed as follows.

- The interfacial void length distribution in 3D printed concrete is quasi-exponential such that the probability decreases exponentially against the void length when the void length is greater than two times the node interval of material surface.

- A smaller void ratio results in a higher descent rate with a shorter tail in the void length distribution, while a larger void ratio results in a lower descent rate with a longer tail. The void ratio and descent rate are correlated through normal cumulative distribution functions.

- The surface node interval serves as a horizontal scaling factor, with a wider distribution caused by a larger interval and a narrower distribution caused by a smaller interval. The peak of the void length is usually between 0 and 2 times the node interval.

- The node interval can be determined by the modified discrete Fourier transform (mDFT) of the material surface, since the node interval exhibits a linear correlation with the peak point after mDFT.

- The quantity of interfacial voids is symmetric about a void ratio of 0.5 with its maximum equal to 0.25 times the ratio between the interface length and the node interval, and the quantity of interfacial voids approaches 0 as the void ratio tends toward 0 or 1.

452　　　• The interlayer strength of 3D printed concrete is affected by the ratio between the

453　　　　interface length and the node interval, and the interlayer strength decreases against

454　　　　the void ratio in a nonlinear pattern which is well approximated by a combination

455　　　　of the exponential and linear functions.

456　　**Acknowledgements**

462　　**Declaration of interests**

463　　　　The authors declare no competing interests.

464　　**References**

465　　[1] J. Xiao, G. Ji, Y. Zhang, G. Ma, V. Mechtcherine, J. Pan, L. Wang, T. Ding, Z. Duan,
466　　　　S. Du, Large-scale 3D printing concrete technology: Current status and future
467　　　　opportunities, Cem. Concr. Compos., 122 (2021) 104115,
468　　　　https://doi.org/10.1016/j.cemconcomp.2021.104115.

469　　[2] S. Muthukrishnan, S. Ramakrishnan, J. Sanjayan, Technologies for improving
470　　　　buildability in 3D concrete printing, Cem. Concr. Compos., 122 (2021) 104144,
471　　　　https://doi.org/10.1016/j.cemconcomp.2021.104144.

472　　[3] R.A. Buswell, W.R. Leal de Silva, S.Z. Jones, J. Dirrenberger, 3D printing using
473　　　　concrete extrusion: A roadmap for research, Cem. Concr. Res., 112 (2018) 37-49,
474　　　　https://doi.org/10.1016/j.cemconres.2018.05.006.

475　　[4] Y. Han, Z. Yang, T. Ding, J. Xiao, Environmental and economic assessment on 3D

printed buildings with recycled concrete, J. Cleaner Prod., 278 (2021) 123884, https://doi.org/10.1016/j.jclepro.2020.123884.

[5] A. du Plessis, A.J. Babafemi, S.C. Paul, B. Panda, J.P. Tran, C. Broeckhoven, Biomimicry for 3D concrete printing: A review and perspective, Addit. Manuf., 38 (2021) 101823, https://doi.org/10.1016/j.addma.2020.101823.

[6] G. Ma, R. Buswell, W.R. Leal da Silva, L. Wang, J. Xu, S.Z. Jones, Technology readiness: A global snapshot of 3D concrete printing and the frontiers for development, Cem. Concr. Res., 156 (2022) 106774, https://doi.org/10.1016/j.cemconres.2022.106774.

[7] L. Wang, W. Xiao, Q. Wang, H. Jiang, G. Ma, Freeze-thaw resistance of 3D-printed composites with desert sand, Cem. Concr. Compos., 133 (2022), https://doi.org/10.1016/j.cemconcomp.2022.104693.

[8] L. Wang, W. Lin, H. Ma, D. Li, Q. Wang, Mechanical and microstructural properties of 3D-printed aluminate cement based composite exposed to elevated temperatures, Constr. Build. Mater., 353 (2022), https://doi.org/10.1016/j.conbuildmat.2022.129144.

[9] Y. Zhang, H. Qiao, R. Qian, C. Xue, Q. Feng, L. Su, Y. Zhang, G. Liu, H. Du, Relationship between water transport behaviour and interlayer voids of 3D printed concrete, Constr. Build. Mater., 326 (2022) 126731, https://doi.org/10.1016/j.conbuildmat.2022.126731.

[10] L. He, H. Li, W.T. Chow, B. Zeng, Y. Qian, Increasing the interlayer strength of 3D printed concrete with tooth-like interface: An experimental and theoretical investigation, Mater. Des., 223 (2022) 111117, https://doi.org/10.1016/j.matdes.2022.111117.

[11] J.G. Sanjayan, R. Jayathilakage, P. Rajeev, Vibration induced active rheology control for 3D concrete printing, Cem. Concr. Res., 140 (2021) 106293, https://doi.org/10.1016/j.cemconres.2020.106293.

[12] L. He, J.Z.M. Tan, W.T. Chow, H. Li, J. Pan, Design of novel nozzles for higher interlayer strength of 3D printed cement paste, Addit. Manuf., 48 (2021) 102452, https://doi.org/10.1016/j.addma.2021.102452.

[13] T. Ding, J. Xiao, V. Mechtcherine, Microstructure and mechanical properties of interlayer regions in extrusion-based 3D printed concrete: A critical review, Cem. Concr. Compos., 141 (2023) 105154,

[14] L. Ma, Q. Zhang, Z. Jia, C. Liu, Z. Deng, Y. Zhang, Effect of drying environment on mechanical properties, internal RH and pore structure of 3D printed concrete, Constr. Build. Mater., 315 (2022) 125731, https://doi.org/10.1016/j.conbuildmat.2021.125731.

[15] Z. Geng, W. She, W. Zuo, K. Lyu, H. Pan, Y. Zhang, C. Miao, Layer-interface properties in 3D printed concrete: Dual hierarchical structure and micromechanical characterization, Cem. Concr. Res., 138 (2020) 106220, https://doi.org/10.1016/j.cemconres.2020.106220.

[16] S. Yu, M. Xia, J. Sanjayan, L. Yang, J. Xiao, H. Du, Microstructural characterization of 3D printed concrete, J. Build. Eng., 44 (2021) 102948, https://doi.org/10.1016/j.jobe.2021.102948.

[17] Y. Chen, Y. Zhang, Y. Xie, Z. Zhang, N. Banthia, Unraveling pore structure alternations in 3D-printed geopolymer concrete and corresponding impacts on macro-properties, Addit. Manuf., 59 (2022) 103137, https://doi.org/10.1016/j.addma.2022.103137.

[18] J. Kruger, A. du Plessis, G. van Zijl, An investigation into the porosity of extrusion-based 3D printed concrete, Addit. Manuf., 37 (2021) 101740, https://doi.org/10.1016/j.addma.2020.101740.

[19] Y. Chen, O. Çopuroğlu, C. Romero Rodriguez, F.F.d. Mendonca Filho, E. Schlangen, Characterization of air-void systems in 3D printed cementitious materials using optical image scanning and X-ray computed tomography, Mater. Charact., 173 (2021) 110948, https://doi.org/10.1016/j.matchar.2021.110948.

[20] H. Liu, C. Liu, G. Bai, Y. Wu, C. He, R. Zhang, Y. Wang, Influence of pore defects on the hardened properties of 3D printed concrete with coarse aggregate, Addit. Manuf., 55 (2022) 102843, https://doi.org/10.1016/j.addma.2022.102843.

[21] J. Kruger, G. van Zijl, A compendious review on lack-of-fusion in digital concrete fabrication, Addit. Manuf., 37 (2021) 101654, https://doi.org/10.1016/j.addma.2020.101654.

[22] B. Panda, S. Ruan, C. Unluer, M.J. Tan, Investigation of the properties of alkali-activated slag mixes involving the use of nanoclay and nucleation seeds for 3D printing, Compos. Part B-Eng., 186 (2020) 107826, https://doi.org/10.1016/j.compositesb.2020.107826.

[23] B. Panda, N.A. Noor Mohamed, S.C. Paul, G. Bhagath Singh, M.J. Tan, B. Savija, The Effect of Material Fresh Properties and Process Parameters on Buildability and Interlayer Adhesion of 3D Printed Concrete, Materials, 12 (2019) 31277393, https://doi.org/10.3390/ma12132149.

[24] M. van den Heever, A. du Plessis, J. Kruger, G. van Zijl, Evaluating the effects of porosity on the mechanical properties of extrusion-based 3D printed concrete, Cem. Concr. Res., 153 (2022) 106695, https://doi.org/10.1016/j.cemconres.2021.106695.

[25] B. Zhu, J. Pan, J. Li, P. Wang, M. Zhang, Relationship between microstructure and

strain-hardening behaviour of 3D printed engineered cementitious composites, Cem. Concr. Compos., 133 (2022) 104677, https://doi.org/10.1016/j.cemconcomp.2022.104677.

[26] A. Das, Y. Song, S. Mantellato, T. Wangler, D.A. Lange, R.J. Flatt, Effect of processing on the air void system of 3D printed concrete, Cem. Concr. Res., 156 (2022) 106789, https://doi.org/10.1016/j.cemconres.2022.106789.

[27] G. Zhao, H. Gao, Z. Qu, H. Fan, H. Meng, Anhydrous interfacial polymerization of sub-1 Å sieving polyamide membrane, Nat. Commun., 14 (2023) 7624, https://doi.org/10.1038/s41467-023-43291-2.

[28] Q. Shen, Q. Song, Z. Mai, K.-R. Lee, T. Yoshioka, K. Guan, R.R. Gonzales, H. Matsuyama, When self-assembly meets interfacial polymerization, Sci. Adv., 9 (2023) eadf6122, https://doi.org/10.1126/sciadv.adf6122.

[29] Y. Chen, Y. Li, Y. Li, J. Guo, S. Li, S. Zhang, Nano-Interlayers Fabricated via Interfacial Azo-Coupling Polymerization: Effect of Pore Properties of Interlayers on Overall Performance of Thin-Film Composite for Nanofiltration, ACS Appl. Mater. Interfaces, 13 (2021) 59329-59340, https://doi.org/10.1021/acsami.1c19525.

[30] D. Verma, P. Kumar, S. Mukherjee, D. Thakur, C.V. Singh, V. Balakrishnan, Interplay between Thermal Stress and Interface Binding on Fracture of WS2 Monolayer with Triangular Voids, ACS Appl. Mater. Interfaces, 14 (2022) 16876-16884, https://doi.org/10.1021/acsami.2c00901.

[31] T. Marchment, J. Sanjayan, M. Xia, Method of enhancing interlayer bond strength in construction scale 3D printing with mortar by effective bond area amplification, Mater. Des., 169 (2019) 107684, https://doi.org/10.1016/j.matdes.2019.107684.

[32] H. Wang, J. Shao, J. Zhang, D. Zou, X. Sun, Bond shear performances and constitutive model of interfaces between vertical and horizontal filaments of 3D printed concrete, Constr. Build. Mater., 316 (2022), https://doi.org/10.1016/j.conbuildmat.2021.125819.

[33] L. He, W.T. Chow, H. Li, Effects of interlayer notch and shear stress on interlayer strength of 3D printed cement paste, Addit. Manuf., 36 (2020) 101390, https://doi.org/10.1016/j.addma.2020.101390.

[34] J. Xiao, H. Liu, T. Ding, Finite element analysis on the anisotropic behavior of 3D printed concrete under compression and flexure, Addit. Manuf., 39 (2021) 101712, https://doi.org/10.1016/j.addma.2020.101712.

[35] M. van den Heever, F. Bester, J. Kruger, G. van Zijl, Numerical modelling strategies for reinforced 3D concrete printed elements, Addit. Manuf., 50 (2022) 102569, https://doi.org/10.1016/j.addma.2021.102569.

[36] Y. Chen, Z. Chang, S. He, O. Çopuroğlu, B. Šavija, E. Schlangen, Effect of curing methods during a long time gap between two printing sessions on the interlayer bonding of 3D printed cementitious materials, Constr. Build. Mater., 332 (2022) 127394, https://doi.org/10.1016/j.conbuildmat.2022.127394.

[37] L. Feng, G. Mi, X. Shi, M. You, J. Yang, G. Qin, G. Sun, Q. Chen, Tough Interfacial Adhesion Enabled Extremely Durable Flexible Supercapacitors, ACS Appl. Mater. Interfaces, 15 (2023) 53951-53964, https://doi.org/10.1021/acsami.3c12784.

[38] M. Kachanov, Elastic solids with many cracks: A simple method of analysis, Int. J. Solids Struct., 23 (1987) 23-43, https://doi.org/10.1016/0020-7683(87)90030-8.

[39] H.R. Millwater, A simple and accurate method for computing stress intensity factors of collinear interacting cracks, Aerosp. Sci. Technol., 14 (2010) 542-550, https://doi.org/10.1016/j.ast.2010.04.003.

[40] F.N. Schmidt, E.A. Zimmermann, F. Walsh, C. Plumeyer, E. Schaible, I.A.K. Fiedler, P. Milovanovic, M. Rößle, M. Amling, C. Blanchet, B. Gludovatz, R.O. Ritchie, B. Busse, On the Origins of Fracture Toughness in Advanced Teleosts: How the Swordfish Sword's Bone Structure and Composition Allow for Slashing under Water to Kill or Stun Prey, Adv. Sci., 6 (2019) 1900287, https://doi.org/10.1002/advs.201900287.

[41] W.S. Lei, Z. Yu, A statistical approach to scaling size effect on strength of concrete incorporating spatial distribution of flaws, Constr. Build. Mater., 122 (2016) 702-713, https://doi.org/10.1016/j.conbuildmat.2016.06.102.